

THE BOSS EMISSION-LINE LENS SURVEY. III. :
STRONG LENSING OF Ly α EMITTERS BY INDIVIDUAL GALAXIES

YIPING SHU^{1, 2}, ADAM S. BOLTON^{2, 3}, CHRISTOPHER S. KOCHAN⁴, MASAMUNE OGURI^{5, 6, 7}, ISMAEL PÉREZ-FOURNON^{8, 9},
ZHENG ZHENG², SHUDE MAO^{1, 10, 11}, ANTONIO D. MONTERO-DORTA², JOEL R. BROWNSTEIN², RUI MARQUES-CHAVES^{8, 9},
AND BRICE MÉNARD¹²

Draft version July 26, 2016

ABSTRACT

We introduce the Baryon Oscillation Spectroscopic Survey (BOSS) Emission-Line Lens Survey (BELLS) for GALaxy-Ly α EmitteR sYstems (BELLS GALLERY) Survey, which is a Hubble Space Telescope program to image a sample of galaxy-scale strong gravitational lens candidate systems with high-redshift Ly α emitters (LAEs) as the background sources. The goal of the BELLS GALLERY Survey is to illuminate dark substructures in galaxy-scale halos by exploiting the small-scale clumpiness of rest-frame far-UV emission in lensed LAEs, and to thereby constrain the slope and normalization of the substructure-mass function. In this paper, we describe in detail the spectroscopic strong-lens selection technique, which is based on methods adopted in the previous Sloan Lens ACS (SLACS) Survey, BELLS, and SLACS for the Masses Survey. We present the BELLS GALLERY sample of the 21 highest-quality galaxy–LAE candidates selected from $\approx 1.4 \times 10^6$ galaxy spectra in the BOSS of the Sloan Digital Sky Survey III. These systems consist of massive galaxies at redshifts of approximately 0.5 strongly lensing LAEs at redshifts from 2–3. The compact nature of LAEs makes them an ideal probe of dark substructures, with a substructure-mass sensitivity that is unprecedented in other optical strong-lens samples. The magnification effect from lensing will also reveal the structure of LAEs below 100 pc scales, providing a detailed look at the sites of the most concentrated unobscured star formation in the universe. The source code used for candidate selection is available for download as a part of this release.

Subject headings: gravitational lensing: strong—dark matter—galaxies: elliptical and lenticular, cD—
techniques: spectroscopic

1. INTRODUCTION

To date, various observational discoveries including the accelerating expansion of the universe, primordial nucleosynthesis, the structure of the cosmic microwave background, and the large-scale clustering of galaxies support the Λ cold dark matter (Λ CDM)

model as the standard cosmological paradigm (e.g., Riess et al. 1998; Perlmutter et al. 1999; Burles et al. 2001; Anderson et al. 2014; Planck Collaboration et al. 2015). Nevertheless, the nature of dark matter (DM) itself is still mysterious. In particular, analytical calculations and numerical simulations based on the CDM assumption suggest a significant excess in the number of substructures as compared to the observed population of satellite galaxies around the Milky Way (e.g., Klypin et al. 1999; Moore et al. 1999; Bullock 2010; Boylan-Kolchin et al. 2011). Hence, observationally quantifying the abundance and mass function of substructure, especially *dark* substructure, represents an important probe of the nature of DM, and an important test of the favored cosmological model.

Direct observation of dark substructure is by definition limited by its dark nature. As an effect that is directly sensitive to gravity regardless of the electromagnetic radiation, strong gravitational lensing has been shown to be a unique and powerful tool in probing the mass distribution in galaxy and cluster scales (e.g., Bolton et al. 2006a; Koopmans et al. 2006; Treu et al. 2006; Gavazzi et al. 2007; Bolton et al. 2008a; Gavazzi et al. 2008; Bolton et al. 2008b; Treu et al. 2009; Auger et al. 2010; Bolton et al. 2012b; Johnson et al. 2014; Oguri et al. 2014; Sharon et al. 2014; Shu et al. 2015; Wang et al. 2015). In principle, dark substructures within lensing galaxies can induce observationally perceptible signals and therefore be indirectly detected. In particular, perturbations by dark substructure

¹ National Astronomical Observatories, Chinese Academy of Sciences, 20A Datun Road, Chaoyang District, Beijing 100012, China (yiping.shu@nao.cas.cn)

² Department of Physics and Astronomy, University of Utah, 115 South 1400 East, Salt Lake City, UT 84112, USA

³ National Optical Astronomy Observatory, 950 N. Cherry Ave., Tucson, AZ 85719 USA (bolton@noao.edu)

⁴ Department of Astronomy & Center for Cosmology and Astroparticle Physics, Ohio State University, Columbus, OH 43210, USA

⁵ Research Center for the Early Universe, University of Tokyo, 7-3-1 Hongo, Bunkyo-ku, Tokyo 113-0033, Japan

⁶ Department of Physics, University of Tokyo, 7-3-1 Hongo, Bunkyo-ku, Tokyo 113-0033, Japan

⁷ Kavli Institute for the Physics and Mathematics of the Universe (Kavli IPMU, WPI), University of Tokyo, Chiba 277-8583, Japan

⁸ Instituto de Astrofísica de Canarias, C/ Vía Láctea, s/n, 38205 San Cristóbal de La Laguna, Tenerife, Spain

⁹ Universidad de La Laguna, Dpto. Astrofísica, E-38206 La Laguna, Tenerife, Spain

¹⁰ Physics Department and Tsinghua Centre for Astrophysics, Tsinghua University, Beijing 100084, China

¹¹ Jodrell Bank Centre for Astrophysics, School of Physics and Astronomy, The University of Manchester, Oxford Road, Manchester M13 9PL, UK

¹² Department of Physics and Astronomy, Johns Hopkins University, Baltimore, MD 21218, USA

tures on the lensing magnification, which is sensitive to the second derivatives of the lensing potential, can occasionally become very strong. As first discussed by Mao & Schneider (1998), such perturbations on the magnification can be used as an explanation of the flux-ratio anomalies, which is the failure of smooth lens models in recovering the observed flux ratios of some lens systems (e.g., Bradač et al. 2002; Dalal & Kochanek 2002; MacLeod et al. 2013). Note that similar effects can also be caused by low-mass structures along the line of sight (Mao et al. 2004; Metcalf 2005; Xu et al. 2009, 2012, 2015; Inoue 2016). Astrometric perturbations by dark substructures, on the other hand, are usually too small for any substructure inference. If the surface brightness of the source further varies in time, then the time delays between multiple lensed images can be used as an extra test for the presence of substructures (e.g., Keeton & Moustakas 2009).

Nevertheless, for extended static sources, the direct observable is the surface-brightness perturbation, a combination of both astrometric and magnification perturbations. By modeling such surface-brightness perturbations as a result of potential perturbations from dark substructures, recent studies have found strong evidence for the presence of dark substructures in several lensing systems (e.g., Vegetti et al. 2010; Fadely & Keeton 2012; Vegetti et al. 2012; Nierenberg et al. 2014; Hezaveh et al. 2016; Inoue et al. 2016). However, a large sample of such detections is needed for a statistical study of dark substructure.

Motivated by the success of the Sloan Lens ACS Survey (SLACS, Bolton et al. 2006a), the Baryon Oscillation Spectroscopic Survey (BOSS) Emission Line Lens Survey (BELLS, Brownstein et al. 2012), and the SLACS for the Masses Survey (S4TM, Shu et al. 2015) in uncovering significant new strong-lens samples, we initiated the BELLS for the GALaxy-Ly α EmitterR sYstems Survey (the BELLS GALLERY Survey hereafter) for dark-substructure detections in galaxy-scale gravitational lenses with high-redshift Ly α emitters (LAEs) as the lensed sources. The lens candidates of the BELLS GALLERY Survey are spectroscopically selected from the final data release, Data Release 12 (DR12), of the BOSS (Dawson et al. 2013) of the Sloan Digital Sky Survey III (SDSS-III, Eisenstein et al. 2011), using selection techniques similar to those employed in the SLACS, BELLS, and S4TM surveys. A Hubble Space Telescope (*HST*) follow-up imaging program has been approved and the observations are currently underway (*HST* Cycle 23, GO Program # 14189, PI: A. S. Bolton). The candidate systems are massive galaxies at redshifts of approximately 0.5, whose BOSS spectra show Ly α emission from more distant LAEs at redshifts of 2–3.

Extensive studies have demonstrated that the lower-mass limit of substructures that can produce observable lensing signals is related to the characteristic size of the lensed source, with smaller sources being sensitive to perturbations by smaller mass substructures (e.g., Schneider et al. 1992; Koopmans & de Bruyn 2000; Moustakas & Metcalf 2003; Kochanek & Dalal 2004; Mortonson et al. 2005; Amara et al. 2006). This is intuitively understandable by noting that smaller lensing masses have smaller associated lensing deflection angles,

and lensed sources with smaller-scale structures subtending smaller angles will be correspondingly sensitive to the effects of these smaller lensing masses. Furthermore, as discussed by Moustakas & Metcalf (2003), the “cut-off” mass can be estimated as $m_c \propto \ell_s^{3/2}$, where ℓ_s is the characteristic length scale of the lensed source. When observed at optical wavelengths, high-redshift LAEs will show structure on small scales corresponding to the far-UV emission from intense localized regions of star formation. Lensed LAEs can hence push the detection limit of dark substructure down by roughly an order of magnitude in terms of its mass when comparing to the currently existing galaxy–galaxy lens samples in which the typical source size is a few times larger. Importantly, this lower-mass detection threshold can also raise the number of expected substructure detections, since lower-mass dark substructures are predicted to be significantly more abundant than higher mass substructures (e.g., Bullock et al. 2001; De Lucia et al. 2004; Gao et al. 2004; van den Bosch et al. 2005; Zentner et al. 2005; Giocoli et al. 2008). Additionally, the capability of detecting low-mass dark substructures is crucial for constraining the nature of DM because the differences in substructure properties predicted by CDM and other alternatives such as warm and self-interacting DM become significantly larger for lower substructure masses (e.g., Colín et al. 2000; Spergel & Steinhardt 2000; Avila-Reese et al. 2001; Springel et al. 2008; Lovell et al. 2012, 2014; Bose et al. 2016).

The sample of lensed LAEs to be delivered by the BELLS GALLERY Survey will also be an invaluable resource for the study of high-redshift LAEs themselves. LAEs are believed to be young, low-mass, extremely star-forming galaxies that serve as the progenitors of modern massive galaxies. They hold clues to the formation and evolution of galaxies at the time when the universe was still young. They can be used as tracers of the large-scale structure to constrain cosmological parameters (e.g., Hill et al. 2008), and as a probe of the high-redshift intergalactic medium even across the reionization epoch (e.g., Miralda-Escudé & Rees 1998; Malhotra & Rhoads 2004; Zheng et al. 2010, 2011). The magnification effect of gravitational lensing in this new sample provides a “cosmic telescope” for these objects, allowing us to probe their detailed structure below 100 pc scales, which are otherwise beyond current observational capabilities.

This paper describes the candidate selection strategy and presents the catalog of the 21 highest-quality galaxy–LAE lens candidate systems being observed by *HST*, along with their properties as measured by the BOSS survey. Subsequent papers in this series will present the results of the *HST* program.

The outline of this paper is as follows. Section 2 describes in detail the lens candidate selection technique adopted for the BELLS GALLERY Survey. Spectroscopic and photometric properties of the 21 highest-quality galaxy–LAE lens candidates are presented in Section 3. Strong-lensing probability is discussed in Section 4. Discussions on the unique studies enabled by this galaxy–LAE lens sample are given in Section 5. The final conclusion is in Section 6.

2. LENS CANDIDATE IDENTIFICATION

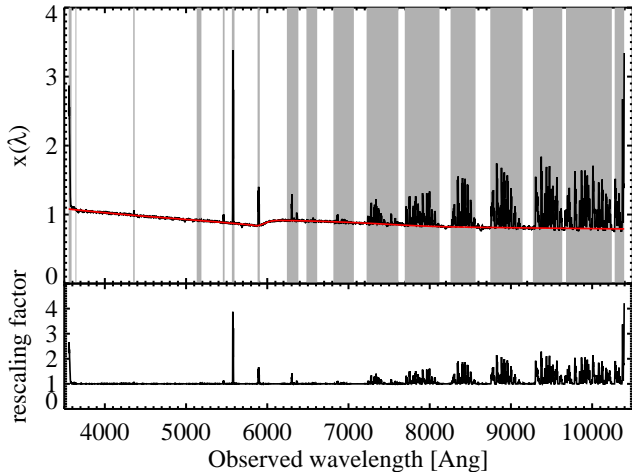


FIG. 1.— Top: error-weighted sky residual RMS spectrum (in black) and the B-spline fit (in red); Bottom: derived factor for error rescaling. The gray-shaded regions in the top panel indicate the masked wavelength ranges during the B-spline fit.

The selection technique for the BELLS GALLERY Survey is based on the technique employed in the previous SLACS, BELLS, and the S4TM surveys, but with substantial modifications to specifically select lensed high-redshift LAEs. The basic principle of the selection technique is to identify a “rogue” emission line in the spectrum of a BOSS survey target galaxy, which can be an indication of a lensing configuration with two objects along the same line of sight. A detailed description of the selection technique adopted for the BELLS GALLERY Survey is presented in this section. This technique is implemented by code that is released publicly with the publication of this paper.

2.1. Flux-error Rescaling

To ensure an accurate quantification of the detection significance of candidate rogue emission lines, the first step is to obtain an accurate estimate of the spectroscopic flux errors across the observed spectra. The BOSS spectroscopic pipeline reports noise vectors that are reasonably accurate at most wavelengths, but underestimate the effects of systematic sky-subtraction residuals at wavelengths with strong airglow lines. Therefore, we recalibrate the reported noise vectors empirically using the sky-subtracted data for the ~ 100 blank-sky fibers on every BOSS spectroscopic plate.

We define the parent sample for our search by selecting all plates with “good” quality (as indicated by the PLATEQUALITY flag in SDSS terminology). For each of these plates, we select all the sky-model-subtracted blank-sky spectra. We reject from our parent sample any plates that have a root mean square (RMS) error-scaled residual flux across all sky spectra of 1.4 or greater, taking this as an indication of unusually poor sky subtraction. This RMS statistic would in principle be 1 for all spectra if all noise were Gaussian, all errors were correctly estimated, and all sky foregrounds were perfectly subtracted.

We then compute the RMS of the error-weighted blank-sky residuals across all retained plates at each wavelength. The result is a spectrum of empirical values $x(\lambda)$ (the black line in the top panel of Figure 1) indicat-

ing the factor by which errors are underestimated as a function of wavelength. The easiest procedure for applying this spectrum would be to simply inflate all reported errors by this wavelength-dependent factor x . However, in some spectral ranges that are relatively free of sky emission lines, the RMS error-weighted residual flux is less than unity as a result of spectral rebinning effects. Since we wish to be conservative in our estimates of detection significance and not *deflate* any error estimates, we fit a smooth B-spline model to the baseline trend of $x(\lambda)$, masking the spectral ranges that are significantly affected by airglow lines. The red line in the top panel of Figure 1 represents the B-spline fit, and the gray-shaded regions visualize the masked spectral ranges. We divide $x(\lambda)$ by this baseline fit to obtain the factor by which we rescale all our error estimates in subsequent analysis steps. The bottom panel in Figure 1 shows the resulting rescaling factor as a function of wavelength. Note that the rescaling factors are forced to be at least unity.

2.2. Emission-line Search

After applying our flux-error rescaling, we search for rogue emission lines in the spectra of galaxies. The $\sim 1.5 \times 10^6$ optical galaxy spectra in the SDSS-III BOSS database, with resolution $R \approx 2000$ and wavelength coverage from 3500 to 10,400 Å, provide an unmatched sample for this search. We select the subset from the BOSS final data release, DR12, that have confidently measured redshifts and classifications as galaxies according to the automated analysis pipeline (Bolton et al. 2012a). That results in 1,388,190 records. We subtract from each spectrum the pipeline’s best-fit galaxy template to obtain the galaxy-subtracted residual spectrum. We then perform an error-weighted matched-filter search within the galaxy-subtracted residual spectrum with a Gaussian kernel of 150 km s^{-1} dispersion, and retain detections (“hits”) of $6\text{-}\sigma$ significance (signal-to-noise ratio, SNR) and above (Bolton et al. 2004). We confine our search to the observed wavelength range $3600 \text{ \AA} < \lambda < 4800 \text{ \AA}$ (roughly $2 < z < 3$ for the Ly α emission) so that low-redshift H α , [OIII] 5007, and H β cannot be detected as interlopers masquerading as high-redshift Ly α . This procedure identifies 4982 hits in total.

2.3. False Positives Removal

We apply several restrictive cuts to remove spurious detections. We first reject any significant overdensities of hits in both observed wavelength (associated with airglow features) and BOSS target-galaxy rest wavelength (associated with template-subtraction residuals). This cut removes almost 65% (3212) of the total 4982 hits. To reject low-redshift [OII] 3727 interlopers, we compute emission-line detection significance at wavelength positions that would correspond to H α , [OIII] 5007, and H β if the primary “hit” were [OII] 3727 instead of Ly α . We drop any hit for which the quadrature sum of SNR values at these three wavelength positions is greater than 2.5σ . This step further removes 845 hits. We then fit the spectrum of each remaining emission-line hit with a pixel-integrated skew-normal profile (Gaussian times error function) in order to quantify the line flux, line width, and skewness. The spectra of all 290 hits with significance greater than 8σ are inspected visually, to re-

TABLE 1
SELECTED PROPERTIES OF THE 21 GALAXY-LAE LENS CANDIDATE SYSTEMS.

Target	Plate-MJD-Fiber	z_L	z_s	R.A.	Decl.	m_i^a	$\text{Ly}\alpha$ Flux ^b
SDSS J002927.38+254401.7	6281-56295-811	0.5869	2.4504	00 29 27.3883	+25 44 01.7862	19.22	32.88
SDSS J005409.97+294450.8	6254-56268- 35	0.4488	2.7176	00 54 09.9754	+29 44 50.8882	19.53	26.48
SDSS J011300.57+025046.2	4315-55503-703	0.6230	2.6088	01 13 00.5750	+02 50 46.2048	19.45	29.66
SDSS J020121.39+322829.6 ^c	6605-56565-722	0.3957	2.8209	02 01 21.3954	+32 28 29.6649	18.32	26.43
SDSS J023740.63-064112.9	4399-55811-149	0.4859	2.2491	02 37 40.6393	-06 41 12.9900	19.22	32.27
SDSS J074249.68+334148.9	4440-55539- 41	0.4936	2.3633	07 42 49.6857	+33 41 48.9890	19.47	45.40
SDSS J075523.52+344539.5 ^c	3754-55488-639	0.7224	2.6347	07 55 23.5254	+34 45 39.5920	20.54	11.29
SDSS J085621.59+201040.5	5175-55955-755	0.5074	2.2335	08 56 21.5918	+20 10 40.5510	19.44	33.56
SDSS J091807.86+451856.7	5813-56363-341	0.5238	2.3440	09 18 07.8662	+45 18 56.7691	19.35	35.83
SDSS J091859.21+510452.5 ^d	5730-56607-697	0.5811	2.4030	09 18 59.2126	+51 04 52.5934	19.71	22.93
SDSS J111027.11+280838.4	6435-56341-855	0.6073	2.3999	11 10 27.1106	+28 08 38.4654	19.91	28.65
SDSS J111040.42+364924.4	4622-55629-615	0.7330	2.5024	11 10 40.4260	+36 49 24.3997	19.86	33.18
SDSS J111634.55+091503.0	5369-56272-541	0.5501	2.4536	11 16 34.5593	+09 15 03.0453	19.40	46.61
SDSS J114154.71+221628.8	6422-56328-303	0.5858	2.7624	11 41 54.7119	+22 16 28.8931	19.73	20.34
SDSS J120159.02+474323.2 ^d	6672-56386-474	0.5628	2.1258	12 01 59.0259	+47 43 23.1967	19.30	182.01
SDSS J122656.45+545739.0	6833-56413-181	0.4980	2.7322	12 26 56.4587	+54 57 39.0454	18.88	36.71
SDSS J151641.22+495440.7	6727-56369-967	0.5479	2.8723	15 16 41.2207	+49 54 40.7785	19.02	32.68
SDSS J152926.41+401548.8	5165-56063-315	0.5308	2.7920	15 29 26.4148	+40 15 48.8480	19.35	30.87
SDSS J222825.76+120503.9	5048-56218-801	0.5305	2.8324	22 28 25.7666	+12 05 03.9505	19.89	24.36
SDSS J224505.93+004018.3	4205-55454-645	0.7021	2.5413	22 45 05.9326	+00 40 18.3506	19.56	27.21
SDSS J234248.68-012032.5	4356-55829-547	0.5270	2.2649	23 42 48.6841	-01 20 32.5351	19.57	54.95

a: BOSS-measured i -band apparent model magnitude within the $1''$ fiber.

b: Total apparent flux of the $\text{Ly}\alpha$ emission in units of $10^{-17} \text{ erg cm}^{-2} \text{ s}^{-1}$.

c: Two systems with strong evidence for lensing signals in their SDSS images. Please see Section 3.2 for details.

d: Two systems with probable evidence for lensing signals in their SDSS images. Please see Section 3.2 for details.

ject detections that are associated with either the subtraction of an incorrect redshift template or cross-talk from a neighboring spectrum on the CCD detector. The procedure yields a final parent sample of 187 candidate systems, which are further inspected by (1) examining their individual 15-minute sub-exposure spectra in order to ensure that the detection does not come from one sub-exposure alone, (2) examining the raw spectrograph CCD frames to ensure that the detections are not associated with cosmetic CCD defects, (3) examining the flat-fielding calibration vectors applied to the spectra at the wavelength of the detection, to ensure that no flat-fielding artifacts have been imprinted onto the spectra, and (4) examining their SDSS color images. None of the remaining systems are rejected by these final checks.

2.4. Final Sample for HST Follow-up

To make the best use of *HST* time and maximize the detection success rate, a highest-quality subsample was selected from the final parent sample. We first restrict the foreground lens to be a BOSS CMASS galaxy. The detailed magnitude and color cuts used for the classifications of CMASS and LOWZ galaxies can be found in (Shu et al. 2012; Dawson et al. 2013). The subsample of candidates that we propose for *HST* observation are selected to have a detection significance of 15σ or greater, an observed emission-line flux greater than $2 \times 10^{-16} \text{ erg cm}^{-2} \text{ s}^{-1}$, and evidence for positive skewness (the classic $\text{Ly}\alpha$ “blue edge, red tail” profile) of $\Delta\chi^2 > 4$ relative to the best-fit symmetric Gaussian line profile. Two of these purely spectroscopically selected systems also show indications of blue lensed features in the SDSS images. In addition, we also include two systems in the longer candidate list which did not meet these

more stringent spectroscopic requirements but showed obvious signatures of blue lensed features in their SDSS image (See Section 3.2 for details). The list of the final 21 highest-quality galaxy-LAE candidates selected by these final cuts is presented in Table 1.

3. THE BELLS GALLERY SAMPLE

In this section, we present the BOSS-determined spectroscopic and photometric properties of the 21 galaxy-LAE lens candidate systems targeted for *HST* follow-up observations.

3.1. Spectroscopic and Photometric Properties

All but two of our lens candidates are selected purely based on their spectroscopic data. Figure 2 displays the BOSS spectra (in black) observed within the $1''$ -radius fibers for the 21 galaxy-LAE lens candidate systems, with a 5 pixel smoothing applied to suppress noise. We limit the spectra to the observed wavelength range from 3600\AA – 4800\AA . Gray lines show the best-fit template for the continuum of the foreground BOSS galaxy as determined by the BOSS redshift and classification pipeline (Bolton et al. 2012a). Since the foreground galaxies are early-type galaxies (ETGs) at redshift $z \sim 0.5$, there is little detectable foreground-galaxy flux within this wavelength range. All the continuum-subtracted residual spectra of these 21 systems exhibit strong emission features in the selected wavelength window. We attribute the emission lines to the $\text{Ly}\alpha$ emission from high-redshift LAEs that happen to fall directly along the line of sight beyond the targeted BOSS galaxies since we have eliminated other possible line interlopers. Figure 3 presents a zoomed in view of the $\text{Ly}\alpha$ emission lines in the rest frame of the LAEs, ordered by decreasing apparent $\text{Ly}\alpha$

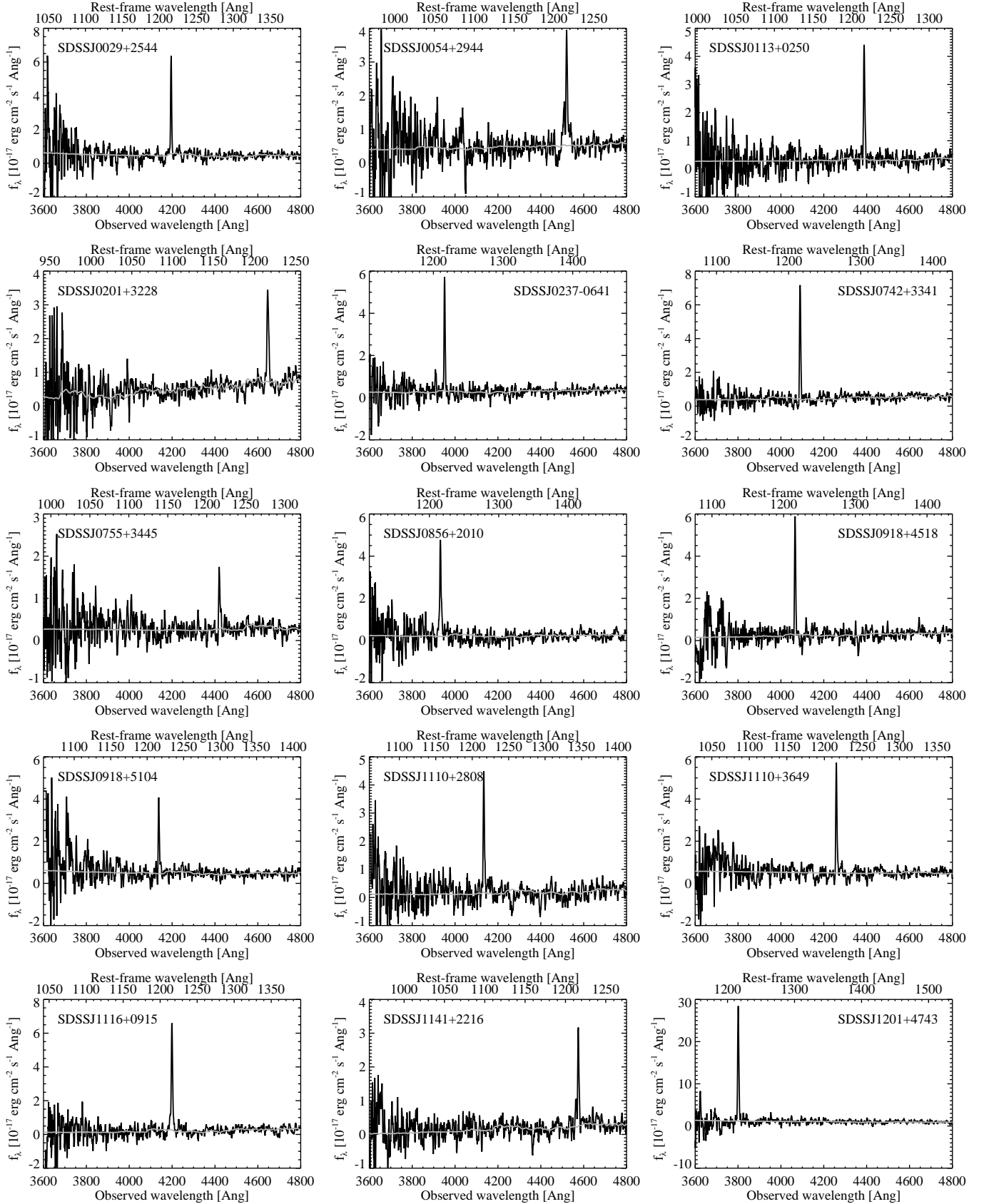


FIG. 2.— Smoothed BOSS spectra of the BELLS GALLERY sample. Gray lines represent the best-fit continuum flux for the foreground galaxies.

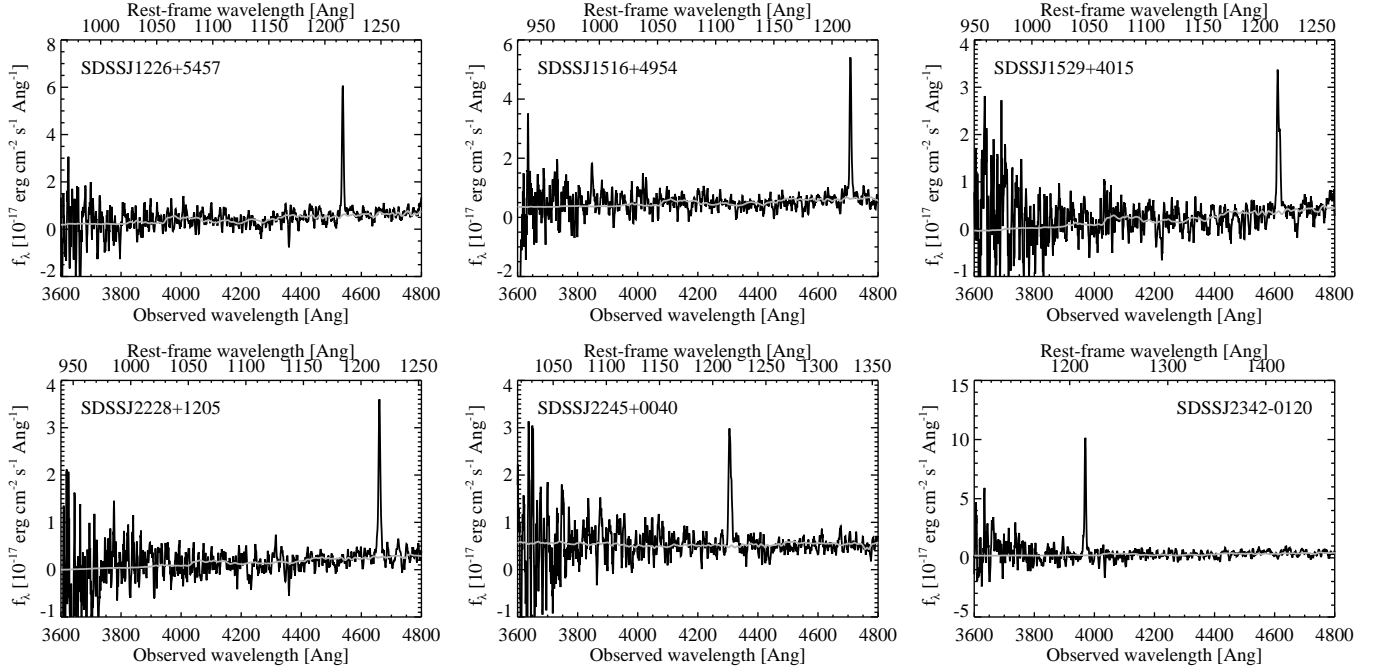
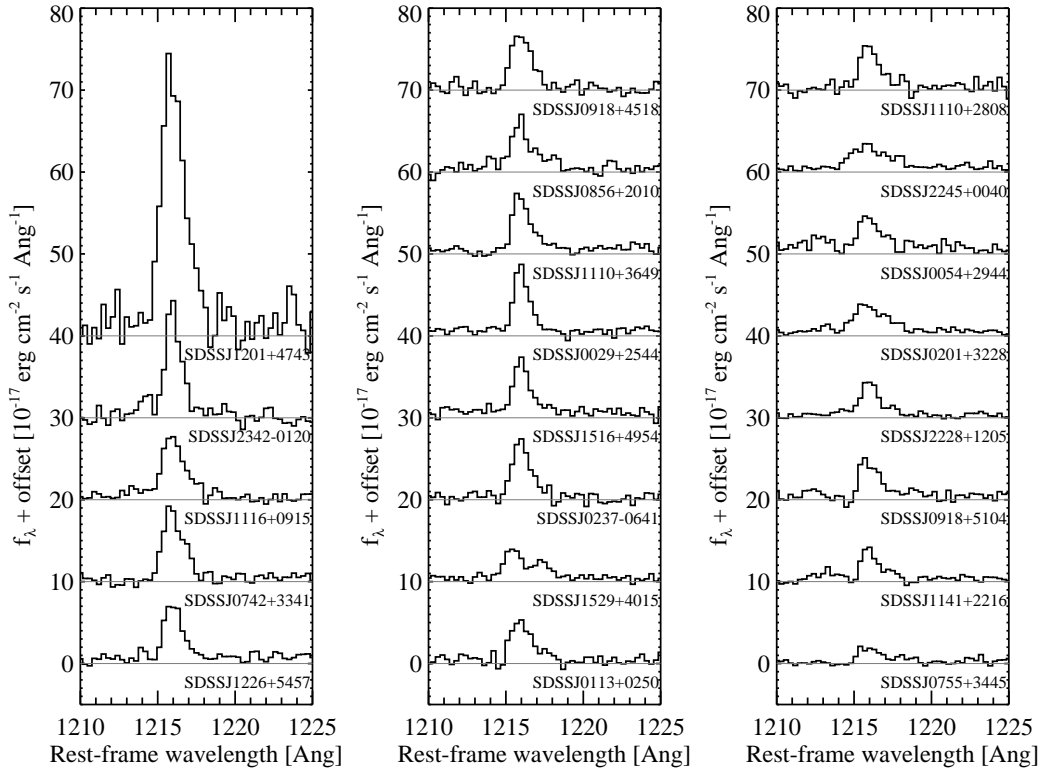
FIG. 2.— *Continued*

FIG. 3.— Zoomed in views of the Ly α emission lines for the BELLS GALLERY sample ordered by decreasing apparent Ly α flux, redshifted to the rest frame of the LAEs. Gray lines are the best-fit continuum flux for the foreground galaxies. Note the “blue edge, red tail” line profiles characteristic of LAEs.

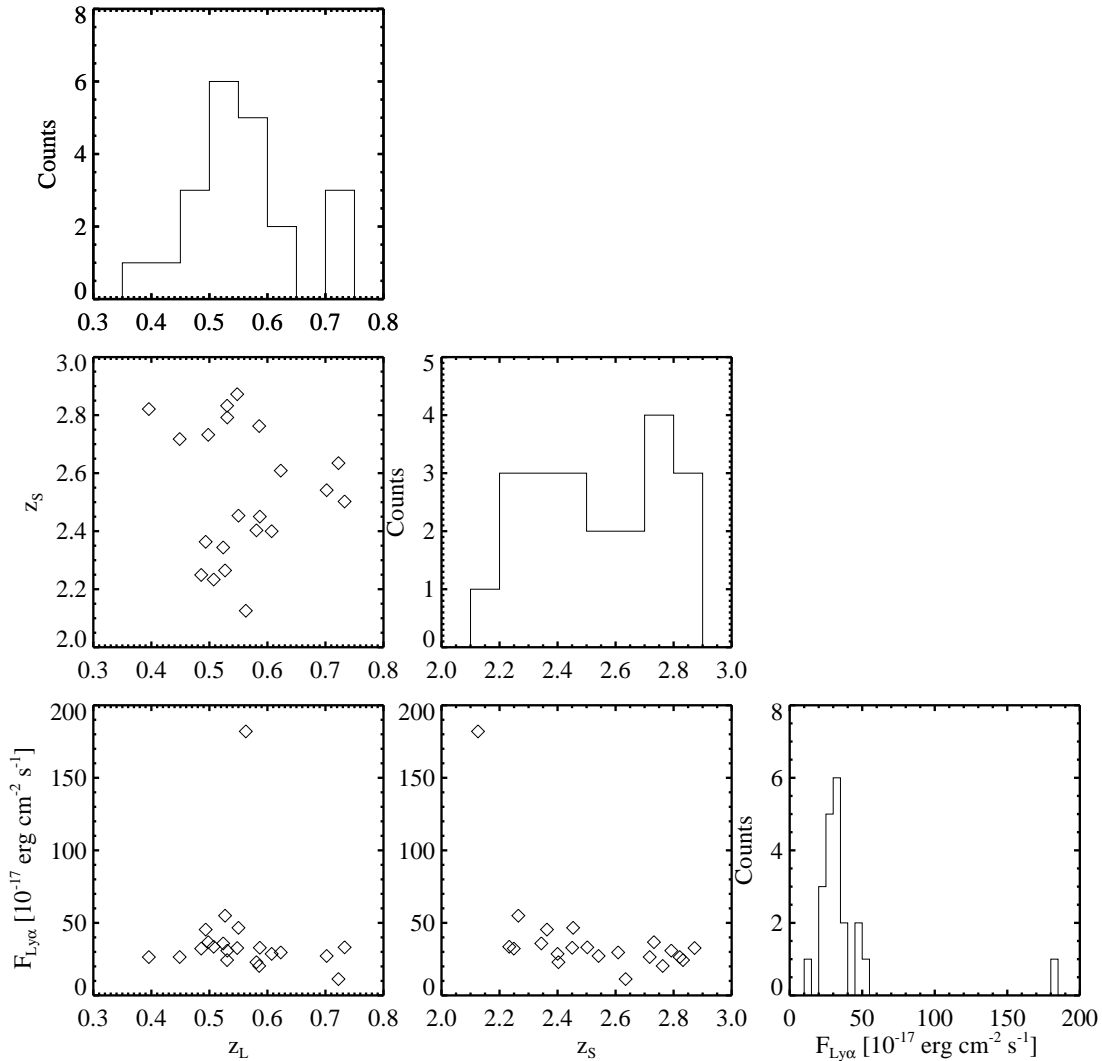


FIG. 4.— Distributions of the BELLS GALLERY sample in various parameter combinations. Histograms of the distributions are shown along the diagonal.

line flux. Note the “blue edge, red tail” line profiles characteristic of LAEs.

Table 1 reports basic spectroscopic and photometric properties of the 21 galaxy–LAE lens candidate systems as measured from SDSS/BOSS data. The redshift of the foreground lens galaxy z_L is measured spectroscopically as explained in Bolton et al. (2012a). The redshift of the lensed LAE z_S can be inferred from the observed Ly α emission. The observed total flux of the Ly α emission $F_{\text{Ly}\alpha}$ is estimated from the corresponding skew-normal fit and listed in units of $10^{-16} \text{ erg cm}^{-2} \text{ s}^{-1}$. As mentioned previously, two of the 21 candidates (asterisked in the table) show definitive evidence for lensing features in their SDSS color images, while another two candidates show probable evidence for lensing features. More details about these four systems will be given in Section 3.2. Table 2 in the Appendix summarizes the same spectroscopic and photometric properties for the remaining 166 galaxy–LAE lens candidate systems in the parent sam-

ple.

Figure 4 shows the distributions of the 21 galaxy–LAE lens candidate systems in the space of redshifts and Ly α flux. The redshift distribution of the foreground galaxies in our sample shows no significant deviation from that of the parent BOSS CMASS galaxy sample from which the candidates are selected (Dawson et al. 2013). The source redshift distribution is relatively flat within $2.1 < z_S < 2.9$, and there is no correlation between z_L and z_S . From the redshift distributions for both the foreground lens and background source, we do not see any significant systematic bias toward a particular redshift range. The observed total flux of the Ly α emission is generally between $2 \times 10^{-16} \text{ erg cm}^{-2} \text{ s}^{-1}$ and $5 \times 10^{-16} \text{ erg cm}^{-2} \text{ s}^{-1}$ except for one (SDSS J1201+4743) with an extremely high flux of $1.8 \times 10^{-15} \text{ erg cm}^{-2} \text{ s}^{-1}$. This highest-flux system also happens to have the closest source ($z_S = 2.1258$). As will be discussed in the following section, this system is one of the two systems with probable strong-lensing features in their SDSS images.

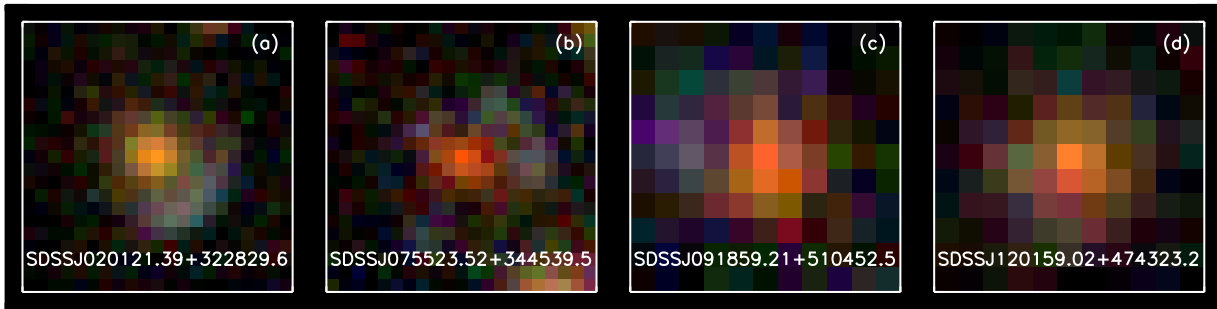


FIG. 5.— Color-composite SDSS images of the four systems with strong (panels (a) and (b)) or probable (panels (c) and (d)) evidence for lensing signals. The first two panels are $4'' \times 4''$, and the other two panels are $2'' \times 2''$. All images are orientated such that north is up and east is to the left.

There is a mild correlation between the source redshift and the total apparent emission-line flux. Note that all flux values are reported here without any correction for lensing magnification or fiber aperture losses.

3.2. Notes on Individual Systems

SDSS J020121.39+322829.6—One of the two systems that exhibit definitive evidence for strong-lensing features in the corresponding color-composite SDSS images. This particular source shows a distinctive, extremely elongated arc with a relatively bluer color to the southwest of the foreground galaxy (panel (a) in Figure 5). Although the foreground galaxy is a LOWZ instead of CMASS galaxy, the presence of the arc makes it an extremely promising candidate, and hence we include it in the *HST* target list.

SDSS J075523.52+344539.5—The other system that shows strong evidence for strong-lensing features in its color-composite SDSS image. Two distinctive bluish blobs connected by an arc are seen to the northwest and west of the foreground galaxy, with another faint blob to the southeast (panel (b) in Figure 5). Although the detection significance and total flux of its emission line does not meet the selection thresholds, we include this system in the sample because of the suggestion of multiply lensed images.

SDSS J091859.21+510452.5—A system that shows probable evidence for strong-lensing features in its color-composite SDSS image. A faint blue/greenish arc-like structure is seen to the northeast of the foreground galaxy (panel (c) in Figure 5).

SDSS J120159.02+474323.2—The system with the highest apparent emission-line flux. Its color-composite SDSS image shows some greenish features surrounding the foreground galaxy as a possible indication of strong lensing (panel (d) in Figure 5).

4. STRONG-LENSING PROBABILITY

For these systems to be powerful scientific tools, they must be bona fide strong lenses. Having applied several restrictive cuts on the significance, flux, and shape of the detected emission line, we are confident about the identification as high-redshift Ly α . In this section we estimate the probability that these LAEs are strongly lensed.

To estimate the rate of strongly lensed LAE events within the sample, we simulate our spectroscopic selection procedures following the Monte Carlo approach of Arneson et al. (2012), with parameters tuned to the

BELLS GALLERY Survey. We model the LAE size distribution using exponential disks with a half-light radius drawn from an exponential distribution of e -folding scale $0''.05$ taken from Bond et al. (2012). We assume that the Ly α emission-line luminosity function has a simple power-law form as

$$n(L, z) \propto L^{-\alpha}, \quad (1)$$

where $n(L, z)$ is the differential number density of LAEs at redshift z with Ly α emission-line luminosity L and α is the power-law index. We take $\alpha \simeq 1.5$ as an approximate average over the faint- and bright-end slopes in the redshift range 2.1–3.1 as studied by Ciardullo et al. (2012). The simulation predicts that essentially all of our detected LAEs will be lensed into multiple images, and that 80%, 50%, and 20% will have total magnifications exceeding 5, 10, and 30, respectively.

As our candidates are selected largely based on the apparent emission-line flux, the magnification effect of gravitational lensing will lead to a so-called magnification bias (e.g., Gott & Gunn 1974; Turner 1980; Vietri & Ostriker 1983), in which the observed number counts of lensed sources in a flux-limited survey will be biased. For the assumed power-law luminosity function, the ratio of the source number counts between the lensed and unlensed scenarios can be estimated as

$$\frac{N(> L_0/\mu)}{N(> L_0)} = \mu^{\alpha-1}, \quad (2)$$

in which $N(> L_0)$ is the total number of LAEs with luminosity greater than L_0 and μ is the average magnification. Taking $\mu = 10$ as a representative value from our simulation, we would expect roughly a factor of 3.2 boost in the number of lensed LAEs relative to the unlensed case.

Given the typical velocity dispersion and redshift of a CMASS galaxy, its multiple imaging cross section at the redshift of the LAE in our sample will be comparable to or larger than the diameter of a BOSS fiber. As a result, the multiply imaged source search region associated with each CMASS galaxy is essentially the size of the fiber. This is very different from general studies of lens statistics (e.g., Kochanek 1993a,b; Maoz & Rix 1993; Jaunsen et al. 1995; Kochanek 1996; King & Browne 1996; Möller et al. 2007) which must account for variations in the multiple imaging cross section with lens redshift, lens mass, and source redshift.

Given this fact, our estimate of the magnification bias

can be checked observationally by comparing the incidence of LAE detections in BOSS galaxy spectroscopic fibers to their incidence within the blank-sky fibers of the survey. To explore this, we rerun the full candidate selection procedure on BOSS sky fibers and obtain 9 candidates with $> 8\text{-}\sigma$ detection significance. This number can be compared to the 187 candidates found to this same significance threshold in the galaxy-fiber sample. Since there are approximately six times more galaxy fibers than sky fibers in the BOSS survey, we find that our high- z LAE detections occur with a frequency $(187/9)/6 \approx 3.5$ times higher in the galaxy fibers than in the sky fibers. This is consistent with the boost factor expected based on our simple magnification-bias calculation above: the higher relative incidence of LAE detections in the galaxy fibers thus suggests that the galaxy-fiber detections are highly magnified by strong lensing. We stress, however, that the close quantitative agreement between the predicted and observed detection-rate boost of galaxy fibers relative to sky fibers must be regarded as coincidental considering the rough approximations involved.

5. DISCUSSION

We first emphasize that our spectroscopic selection technique is powerful and generic, and can be easily applied to a variety of scientific considerations with appropriate modifications. For instance, by changing the single-line detection strategy to detections for at least two of the lines [OII] $\lambda\lambda 3727$, [OIII] 4959, 5007, H α , and H β at a common redshift, one can pick out lens candidates with star-forming galaxies as the background sources. That is exactly the approach adopted in the successful SLACS, BELLS, and S4TM surveys (Bolton et al. 2006a; Brownstein et al. 2012; Shu et al. 2015). One can also specifically search for lensed quasars by tuning the selection criteria to the presence of more than one prominent quasar emission lines such as Ly α , C IV, C III], and Mg II. Interested readers are encouraged to adopt the spectroscopic selection technique according to their own research interests.

Although the size of the sample of galaxy-LAE lenses from our initial *HST* program seems to be relatively modest when compared to other galaxy-scale strong-lens samples, there are another 166 galaxy-LAE lens candidates remaining in the parent sample. We applied very stringent requirements to pick the 21 highest-quality systems for this *HST* program, so many of the remaining 166 systems are also very good lens candidates. Considering the approximately 50% success rates (the ratio of confirmed lenses to selected candidates) in previous spectroscopically selected lens samples in the SLACS, BELLS, and S4TM surveys (Bolton et al. 2008a; Brownstein et al. 2012; Shu et al. 2015), we expect another ~ 80 galaxy-LAE lenses from further follow-ups of the BELLS GALLERY parent sample. The scientific potential for such a large galaxy-LAE sample to constrain the nature and abundance of DM substructure is invaluable.

If the total mass-density profile of a lens galaxy and its DM halo is modeled as a singular isothermal sphere, then the cut-off mass above which substructure lensing effects are observable scales as $m_c \propto \ell_s^{3/2}$, where ℓ_s is the characteristic length scale of the lensed source (Moustakas & Metcalf 2003). Previous works on LAEs

between redshifts 2 and 3 have found a typical size of 1–2 kpc in rest-frame UV light (e.g., Bond et al. 2010; Gronwall et al. 2011; McLinden et al. 2011; Law et al. 2012; Malhotra et al. 2012; Ryan et al. 2012; Bond et al. 2012). More recently, analysis by Shu et al. (2016) of high-resolution *HST* imaging of the lensed $z = 2.7$ LAE system originally described by Bolton et al. (2006b) suggests that the background LAE can even be resolved into three distinct components with characteristic sizes from 116–438 pc. By comparison, the typical physical size of the sources in previously assembled samples of strong galaxy-galaxy lenses (e.g., SLACS, BELLS, and S4TM) is 1–2 kpc (e.g., Newton et al. 2011). Thus, these new galaxy-LAE lens systems have the potential to push the lensing detection limit of DM substructure lower by an order of magnitude.

Certainly, the actual DM substructure detectability depends strongly on the instrumental resolution, sensitivity, and the S/N. Observations in radio/near UV or with the aid of adaptive optics, which in general offer higher resolutions and/or S/Ns relative to the *HST* observations of the BELLS GALLERY sample, are also important for DM substructure detection (e.g., Bradač et al. 2002; Dalal & Kochanek 2002; Vegetti et al. 2012; MacLeod et al. 2013; Nierenberg et al. 2014; Hezaveh et al. 2016; Inoue et al. 2016). Nevertheless, the BELLS GALLERY lens sample itself is invaluable because of its sensitivity to lower-mass substructures than the current strong galaxy-galaxy lenses.

The benefit from this factor of ~ 10 or more boost in the substructure-mass detection limit is threefold. First, lower-mass substructures are much more abundant ($\sim \times 100$) according to the predicted CDM subhalo mass function, which is found to approximately follow a fast-declining power-law profile in semi-analytical models and high-resolution cosmological simulations (e.g., Bullock et al. 2001; De Lucia et al. 2004; Gao et al. 2004; van den Bosch et al. 2005; Zentner et al. 2005; Giocoli et al. 2008). Hence the rate of substructure detection should be higher in this sample than in previous strong-lens samples. Second, sensitivity over a wider range of substructure-masses can lead to constraints on the slope of the substructure mass function in addition to the overall abundance at a given mass. Third, this new sample can probe for the first time the regime in which the predictions of competing DM models differ significantly (e.g., Colín et al. 2000; Spergel & Steinhardt 2000; Avila-Reese et al. 2001; Springel et al. 2008; Lovell et al. 2012, 2014; Li et al. 2015; Bose et al. 2016).

Considering the positive detection of mass substructures in 1/11 galaxy-galaxy lens systems in the Vegetti et al. (2014) analysis, our proposed sample of 21 galaxy-LAE lens systems can be expected to show strong evidence for dark substructure even allowing for the uncertainties in forecasting. We therefore expect this BELLS GALLERY program with 21 galaxy-LAE lens systems to provide the most precise measurement to date of the substructure-mass function in galaxy-scale halos. Alternatively, the non-detection of significant substructure within this new lensed LAE sample would provide surprising evidence for the suppression of low-mass substructure below an unexpectedly high cut-off mass.

A complementary study enabled by this unique sample of galaxy–LAE lens systems is of the mass–density profile of massive ETGs. The foreground lens population in our sample is comparable in all ways to the earlier sample of BELLS lenses, but the higher source redshifts of the LAE lens sample will lead to the formation of lensed images with larger angular Einstein radii. The typical source redshift of BELLS galaxy–galaxy lenses is ~ 1 . Considering a typical BOSS lens galaxy at $z = 0.52$, a $z \sim 3$ LAE will hence correspond to an Einstein radius that is larger by a factor of 1.7. Since gravitational lensing provides a precise mass estimation within the Einstein radius, a combined ensemble analysis of both samples with a range of Einstein radii can provide more precise constraints on the radial mass–density profile in massive ETGs and its decomposition into stars and DM. Other strong-lens programs such as the SDSS Quasar Lens Search (Inada et al. 2012) and the Strong Lensing Legacy Survey (Sonnenfeld et al. 2013) have also found lenses with similar lens and source redshifts. However, their lens selection functions and hence lens populations are different from the BELLS survey, and thereby cannot be directly combined with BELLS lenses as the BELLS GALLERY lenses can.

In addition to the explorations of the foreground lens galaxies, this new sample will enable other studies of high-redshift LAEs. Direct observations of high-redshift LAEs are severely limited by S/N and resolution and therefore strongly biased toward the luminous end. In many cases a stacking technique must be adopted to compensate for low photon counts, and can only provide a rough picture of the entire LAE sample (e.g., Steidel et al. 2011; Matsuda et al. 2012; Feldmeier et al. 2013). Exploration of detailed structures of individual LAEs is challenging and sometimes impossible. Strong gravitational lensing aids in the study of high-redshift LAEs through its magnification effect, in which the apparent size of the lensed source is magnified up to factors of tens (e.g., Bolton et al. 2006b; Bayliss et al. 2010; Christensen et al. 2012; Jones et al. 2013). Therefore, in combination with the unmatched spatial resolution of *HST*, lensing will allow us to explore the details of LAEs below 100 pc scales and to see a clearer picture of the sites of the most concentrated unobscured star formation in the universe. Additionally, as gravitational lensing preserves source surface brightness, the magnification in size leads to an equal boost in the photon counts, which significantly improves the detectability and precision in flux measurement. This boost also permits the exploration of intrinsically faint LAEs which would otherwise require large investments of time in blank-field searches. Once the detailed selection function of our lensed LAE survey is understood through *HST* imaging and spatially resolved ground-based spectroscopy, the full sample of LAEs detected in BOSS spectra can be used for a measurement of the joint size–luminosity function of LAEs and its evolution from $z = 3$ to 2.

Our program will have important implications as a pathfinder for more ambitious lensed LAE surveys within BOSS, and for future spectroscopic projects such as DESI (Flaugher & Bebek 2014) and Subaru-PFS (Sugai et al. 2012). Finally, based on the example of SLACS and other samples of significantly new astronomical systems, numerous unanticipated scientific applications will no

doubt arise on the basis of this new lens sample.

6. CONCLUSION

We have presented a catalog of 21 galaxy–LAE lens candidate systems as a part of the BELLS GALLERY Survey, the goal of which is to “illuminate” dark substructures in galaxy-scale systems and deliver new constraints on the nature of DM and its dynamics. The selection strategy is analogous to the technique adopted in the successful SLACS, BELLS, and S4TM surveys, modified to detect lensed high-redshift LAEs as the background sources. Benefiting from the compact nature of these LAEs, this new sample has the potential to push the lensing detection limit of DM substructure down by an order of magnitude in terms of its mass relative to currently existing galaxy–galaxy lens systems.

The parent sample of 187 galaxy–LAE candidates is selected spectroscopically from the BOSS final data product (DR12) with ≈ 1.4 million galaxy optical spectra by searching for the existence of high-significance Ly α emission in the observed wavelength range of $3600\text{\AA} < \lambda < 4800\text{\AA}$. We also find nine emission-line detections in the BOSS blank sky fibers with the same selection procedures. Such detection enhancement within galaxy fibers is consistent with the lensing magnification-bias effect and the prediction from Monte Carlo simulations that suggest a very high strong-lensing rate in the candidate sample.

By applying multiple quality cuts, we build a final sample of 21 highest-quality galaxy–LAE lens candidate systems for *HST* high-resolution follow-up imaging, which is being carried out under *HST* Cycle 23 GO Program # 14189 (PI: A. S. Bolton). Four of the 21 candidates already exhibit either definitive or probable evidence for lensing features (elongated arc and multiple images) in their SDSS images. The redshift distribution of the lens galaxies is roughly Gaussian, centered at $z \sim 0.5$, with no significant difference from the distribution of redshifts in the parent BOSS CMASS galaxy sample (one candidate is actually a LOWZ galaxy). The background LAEs have a relatively flat redshift distribution from $z = 2.1$ to 2.9, suggesting little selection bias toward any redshift range.

In consideration of a previous detection of dark substructure in the S/N-selected SLACS galaxy–galaxy lens sample (Vegetti et al. 2010), we expect the BELLS GALLERY program and similar programs in the future to illuminate dark substructure within galaxy-scale halos, to provide a precise observational measurement of the substructure-mass function observationally, and to combine with theoretical and numerical predictions to lead to a better understanding of the nature of DM.

Finally, for interested readers, the source code (in Interactive Data Language) implementing the described selection technique can be downloaded from the Bitbucket repository at https://bitbucket.org/abolton/lae_lens. Installation of IDLUTILS, a collection of IDL utilities, is also required and can be done following <http://www.sdss.org/dr12/software/idlutils/>. Our code works specifically with BOSS spectroscopic data which are organized in a particular plate–MJD–fiber structure. Nevertheless, the kernel of the code, the spectroscopic selection technique, is generic and can be

easily adopted to data sets in different structures with moderate modifications.

This work has been partially supported by the Strategic Priority Research Program “The Emergence of Cosmological Structures” of the Chinese Academy of Sciences Grant No. XDB09000000 and by the National Natural Science Foundation of China (NSFC) under grant numbers 11333003 and 11390372 (Y.S. and S.M.). The support and resources from the Center for High Performance Computing at the University of Utah are gratefully acknowledged. The work of M.O. was supported in part by World Premier International Research Center Initiative (WPI Initiative), MEXT, Japan, and JSPS KAKENHI Grant Numbers 26800093 and 15H05892. Z.Z. is partially supported by NASA grant NNX14AC89G and NSF grant AST-1208891.

Funding for SDSS-III was provided by the Alfred P. Sloan Foundation, the Participating Institutions, the National Science Foundation, and the U.S. Department

of Energy Office of Science. The SDSS-III web site is <http://www.sdss3.org/>.

SDSS-III was managed by the Astrophysical Research Consortium for the Participating Institutions of the SDSS-III Collaboration including the University of Arizona, the Brazilian Participation Group, Brookhaven National Laboratory, Carnegie Mellon University, University of Florida, the French Participation Group, the German Participation Group, Harvard University, the Instituto de Astrofísica de Canarias, the Michigan State/Notre Dame/JINA Participation Group, Johns Hopkins University, Lawrence Berkeley National Laboratory, Max Planck Institute for Astrophysics, Max Planck Institute for Extraterrestrial Physics, New Mexico State University, New York University, Ohio State University, Pennsylvania State University, University of Portsmouth, Princeton University, the Spanish Participation Group, University of Tokyo, University of Utah, Vanderbilt University, University of Virginia, University of Washington, and Yale University.

REFERENCES

- Amara, A., Metcalf, R. B., Cox, T. J., & Ostriker, J. P. 2006, *MNRAS*, 367, 1367
- Anderson, L., Aubourg, É., Bailey, S., et al. 2014, *MNRAS*, 441, 24
- Arneson, R. A., Brownstein, J. R., & Bolton, A. S. 2012, *ApJ*, 753, 4
- Auger, M. W., Treu, T., Bolton, A. S., et al. 2010, *ApJ*, 724, 511
- Avila-Reese, V., Colín, P., Valenzuela, O., D’Onghia, E., & Firmani, C. 2001, *ApJ*, 559, 516
- Bayliss, M. B., Wuyts, E., Sharon, K., et al. 2010, *ApJ*, 720, 1559
- Bolton, A. S., Burles, S., Koopmans, L. V. E., et al. 2008a, *ApJ*, 682, 964
- Bolton, A. S., Burles, S., Koopmans, L. V. E., Treu, T., & Moustakas, L. A. 2006a, *ApJ*, 638, 703
- Bolton, A. S., Burles, S., Schlegel, D. J., Eisenstein, D. J., & Brinkmann, J. 2004, *AJ*, 127, 1860
- Bolton, A. S., Moustakas, L. A., Stern, D., et al. 2006b, *ApJ*, 646, L45
- Bolton, A. S., Treu, T., Koopmans, L. V. E., et al. 2008b, *ApJ*, 684, 248
- Bolton, A. S., Schlegel, D. J., Aubourg, É., et al. 2012a, *AJ*, 144, 144
- Bolton, A. S., Brownstein, J. R., Kochanek, C. S., et al. 2012b, *ApJ*, 757, 82
- Bond, N. A., Feldmeier, J. J., Matković, A., et al. 2010, *ApJ*, 716, L200
- Bond, N. A., Gawiser, E., Guaita, L., et al. 2012, *ApJ*, 753, 95
- Bose, S., Hellwing, W. A., Frenk, C. S., et al. 2016, *MNRAS*, 455, 318
- Boylan-Kolchin, M., Bullock, J. S., & Kaplinghat, M. 2011, *MNRAS*, 415, L40
- Bradač, M., Schneider, P., Steinmetz, M., et al. 2002, *A&A*, 388, 373
- Brownstein, J. R., Bolton, A. S., Schlegel, D. J., et al. 2012, *ApJ*, 744, 41
- Bullock, J. S. 2010, *ArXiv e-prints*, arXiv:1009.4505
- Bullock, J. S., Kravtsov, A. V., & Weinberg, D. H. 2001, *ApJ*, 548, 33
- Burles, S., Nollett, K. M., & Turner, M. S. 2001, *Phys. Rev. D*, 63, 063512
- Christensen, L., Laursen, P., Richard, J., et al. 2012, *MNRAS*, 427, 1973
- Ciardullo, R., Gronwall, C., Wolf, C., et al. 2012, *ApJ*, 744, 110
- Colín, P., Avila-Reese, V., & Valenzuela, O. 2000, *ApJ*, 542, 622
- Dalal, N., & Kochanek, C. S. 2002, *ApJ*, 572, 25
- Dawson, K. S., Schlegel, D. J., Ahn, C. P., et al. 2013, *AJ*, 145, 10
- De Lucia, G., Kauffmann, G., Springel, V., et al. 2004, *MNRAS*, 348, 333
- Eisenstein, D. J., Weinberg, D. H., Agol, E., et al. 2011a, *AJ*, 142, 72
- Fadely, R., & Keeton, C. R. 2012, *MNRAS*, 419, 936
- Feldmeier, J. J., Hagen, A., Ciardullo, R., et al. 2013, *ApJ*, 776, 75
- Flaugher, B., & Bebek, C. 2014, in *Proc. SPIE*, Vol. 9147, Ground-based and Airborne Instrumentation for Astronomy V, 91470S
- Gao, L., White, S. D. M., Jenkins, A., Stoehr, F., & Springel, V. 2004, *MNRAS*, 355, 819
- Gavazzi, R., Treu, T., Koopmans, L. V. E., et al. 2008, *ApJ*, 677, 1046
- Gavazzi, R., Treu, T., Rhodes, J. D., et al. 2007, *ApJ*, 667, 176
- Giocoli, C., Tormen, G., & van den Bosch, F. C. 2008, *MNRAS*, 386, 2135
- Gott, III, J. R., & Gunn, J. E. 1974, *ApJ*, 190, L105
- Gronwall, C., Bond, N. A., Ciardullo, R., et al. 2011, *ApJ*, 743, 9
- Hezaveh, Y. D., Dalal, N., Marrone, D. P., et al. 2016, *ArXiv e-prints*, arXiv:1601.01388
- Hill, G. J., Gebhardt, K., Komatsu, E., et al. 2008, in *Astronomical Society of the Pacific Conference Series*, Vol. 399, Panoramic Views of Galaxy Formation and Evolution, ed. T. Kodama, T. Yamada, & K. Aoki, 115
- Inada, N., Oguri, M., Shin, M.-S., et al. 2012, *AJ*, 143, 119
- Inoue, K. T. 2016, *ArXiv e-prints*, arXiv:1601.04414
- Inoue, K. T., Minezaki, T., Matsushita, S., & Chiba, M. 2016, *MNRAS*, 457, 2936
- Jaunsen, A. O., Jablonski, M., Pettersen, B. R., & Stabell, R. 1995, *A&A*, 300, 323
- Johnson, T. L., Sharon, K., Bayliss, M. B., et al. 2014, *ApJ*, 797, 48
- Jones, T. A., Ellis, R. S., Schenker, M. A., & Stark, D. P. 2013, *ApJ*, 779, 52
- Keeton, C. R., & Moustakas, L. A. 2009, *ApJ*, 699, 1720
- King, L. J., & Browne, I. W. A. 1996, *MNRAS*, 282, 67
- Klypin, A., Kravtsov, A. V., Valenzuela, O., & Prada, F. 1999, *ApJ*, 522, 82
- Kochanek, C. S. 1993a, *MNRAS*, 261, 453
- . 1993b, *ApJ*, 417, 438
- . 1996, *ApJ*, 466, 638
- Kochanek, C. S., & Dalal, N. 2004, *ApJ*, 610, 69
- Koopmans, L. V. E., & de Bruyn, A. G. 2000, *A&A*, 358, 793
- Koopmans, L. V. E., Treu, T., Bolton, A. S., Burles, S., & Moustakas, L. A. 2006, *ApJ*, 649, 599
- Law, D. R., Steidel, C. C., Shapley, A. E., et al. 2012, *ApJ*, 759, 29
- Li, R., Frenk, C. S., Cole, S., et al. 2015, *ArXiv e-prints*, arXiv:1512.06507

- Lovell, M. R., Frenk, C. S., Eke, V. R., et al. 2014, *MNRAS*, 439, 300
- Lovell, M. R., Eke, V., Frenk, C. S., et al. 2012, *MNRAS*, 420, 2318
- MacLeod, C. L., Jones, R., Agol, E., & Kochanek, C. S. 2013, *ApJ*, 773, 35
- Malhotra, S., & Rhoads, J. E. 2004, *ApJ*, 617, L5
- Malhotra, S., Rhoads, J. E., Finkelstein, S. L., et al. 2012, *ApJ*, 750, L36
- Mao, S., Jing, Y., Ostriker, J. P., & Weller, J. 2004, *ApJ*, 604, L5
- Mao, S., & Schneider, P. 1998, *MNRAS*, 295, 587
- Maoz, D., & Rix, H.-W. 1993, *ApJ*, 416, 425
- Matsuda, Y., Yamada, T., Hayashino, T., et al. 2012, *MNRAS*, 425, 878
- McLinden, E. M., Finkelstein, S. L., Rhoads, J. E., et al. 2011, *ApJ*, 730, 136
- Metcalf, R. B. 2005, *ApJ*, 629, 673
- Miralda-Escudé, J., & Rees, M. J. 1998, *ApJ*, 497, 21
- Möller, O., Kitzbichler, M., & Natarajan, P. 2007, *MNRAS*, 379, 1195
- Moore, B., Ghigna, S., Governato, F., et al. 1999, *ApJ*, 524, L19
- Mortonson, M. J., Schechter, P. L., & Wambsganss, J. 2005, *ApJ*, 628, 594
- Moustakas, L. A., & Metcalf, R. B. 2003, *MNRAS*, 339, 607
- Newton, E. R., Marshall, P. J., Treu, T., et al. 2011, *ApJ*, 734, 104
- Nierenberg, A. M., Treu, T., Wright, S. A., Fassnacht, C. D., & Auger, M. W. 2014, *MNRAS*, 442, 2434
- Oguri, M., Rusu, C. E., & Falco, E. E. 2014, *MNRAS*, 439, 2494
- Perlmutter, S., Aldering, G., Goldhaber, G., et al. 1999, *ApJ*, 517, 565
- Planck Collaboration, Ade, P. A. R., Aghanim, N., et al. 2015, *ArXiv e-prints*, arXiv:1502.01589
- Riess, A. G., Filippenko, A. V., Challis, P., et al. 1998, *AJ*, 116, 1009
- Ryan, Jr., R. E., McCarthy, P. J., Cohen, S. H., et al. 2012, *ApJ*, 749, 53
- Schneider, P., Ehlers, J., & Falco, E. E. 1992, *Gravitational Lenses*, 112, doi:10.1007/978-3-662-03758-4
- Sharon, K., Gladders, M. D., Rigby, J. R., et al. 2014, *ApJ*, 795, 50
- Shu, Y., Bolton, A. S., Moustakas, L. A., et al. 2016, *ApJ*, 820, 43
- Shu, Y., Bolton, A. S., Schlegel, D. J., et al. 2012, *AJ*, 143, 90
- Shu, Y., Bolton, A. S., Brownstein, J. R., et al. 2015, *ApJ*, 803, 71
- Sonnenfeld, A., Gavazzi, R., Suyu, S. H., Treu, T., & Marshall, P. J. 2013, *ApJ*, 777, 97
- Spergel, D. N., & Steinhardt, P. J. 2000, *Physical Review Letters*, 84, 3760
- Springel, V., Wang, J., Vogelsberger, M., et al. 2008, *MNRAS*, 391, 1685
- Steidel, C. C., Bogosavljević, M., Shapley, A. E., et al. 2011, *ApJ*, 736, 160
- Sugai, H., Karoji, H., Takato, N., et al. 2012, in *Proc. SPIE, Vol. 8446, Ground-based and Airborne Instrumentation for Astronomy IV*, 84460Y
- Treu, T., Gavazzi, R., Gorecki, A., et al. 2009, *ApJ*, 690, 670
- Treu, T., Koopmans, L. V., Bolton, A. S., Burles, S., & Moustakas, L. A. 2006, *ApJ*, 640, 662
- Turner, E. L. 1980, *ApJ*, 242, L135
- van den Bosch, F. C., Tormen, G., & Giocoli, C. 2005, *MNRAS*, 359, 1029
- Vegetti, S., Koopmans, L. V. E., Auger, M. W., Treu, T., & Bolton, A. S. 2014, *MNRAS*, 442, 2017
- Vegetti, S., Koopmans, L. V. E., Bolton, A., Treu, T., & Gavazzi, R. 2010, *MNRAS*, 408, 1969
- Vegetti, S., Lagattuta, D. J., McKean, J. P., et al. 2012, *Nature*, 481, 341
- Vietri, M., & Ostriker, J. P. 1983, *ApJ*, 267, 488
- Wang, X., Hoag, A., Huang, K., et al. 2015, *ArXiv e-prints*, arXiv:1504.02405
- Xu, D., Sluse, D., Gao, L., et al. 2015, *MNRAS*, 447, 3189
- Xu, D. D., Mao, S., Cooper, A. P., et al. 2012, *MNRAS*, 421, 2553
- Xu, D. D., Mao, S., Wang, J., et al. 2009, *MNRAS*, 398, 1235
- Zentner, A. R., Berlind, A. A., Bullock, J. S., Kravtsov, A. V., & Wechsler, R. H. 2005, *ApJ*, 624, 505
- Zheng, Z., Cen, R., Trac, H., & Miralda-Escudé, J. 2010, *ApJ*, 716, 574
- . 2011, *ApJ*, 726, 38

APPENDIX

TABLE 2
 SELECTED PROPERTIES OF THE REMAINING 166 GALAXY-LAE LENS CANDIDATE SYSTEM IN THE BELLS GALLERY PARENT SAMPLE.

Target	Plate-MJD-Fiber	z_L	z_s	R.A.		Decl.		m_i	Ly α Flux
SDSSJ001213.49+173537.5	6111-56270-279	0.4911	1.9886	00 12 13.4911	+17 35 37.5687	19.06	53.86		
SDSSJ001620.58-061115.5	7150-56597-586	0.3015	2.3111	00 16 20.5816	-06 11 15.5836	17.74	22.80		
SDSSJ002123.23-042926.1	7037-56570-769	0.5583	2.1453	00 21 23.2327	-04 29 26.1655	19.77	24.14		
SDSSJ003338.97+042734.9	4418-55862-165	0.5264	2.1854	00 33 38.9738	+04 27 34.9358	19.66	25.30		
SDSSJ005753.31+001600.7	4224-55481-929	0.4937	2.6005	00 57 53.3192	+00 16 00.6960	19.19	23.92		
SDSSJ005948.32+160629.4	5705-56194-259	0.5946	2.8324	00 59 48.3202	+16 06 29.4928	20.01	10.43		
SDSSJ010701.12-030830.6	4373-55811-336	0.2452	2.7271	01 07 01.1261	-03 08 30.6677	17.61	19.60		
SDSSJ011120.66-031559.4	4373-55811- 88	0.4480	2.9289	01 11 20.6648	-03 15 59.4154	18.74	13.53		
SDSSJ012233.11-052239.9	7046-56568-101	0.6539	2.2641	01 22 33.1169	-05 22 39.9855	19.80	13.12		
SDSSJ013148.59-053037.6	7048-56575-335	0.4873	2.7885	01 31 48.5934	-05 30 37.6247	19.86	15.61		
SDSSJ013644.87-064656.6	7162-56605-731	0.6686	2.9470	01 36 44.8787	-06 46 56.6904	19.90	11.74		
SDSSJ013914.73+044334.6	4274-55508-850	0.2437	2.3991	01 39 14.7350	+04 43 34.6793	17.30	31.43		
SDSSJ014526.41-050035.5	7050-56573-273	0.5696	2.7219	01 45 26.4148	-05 00 35.5906	19.95	15.16		
SDSSJ014631.97-012514.6	4350-55556-945	0.5213	2.6038	01 46 31.9762	-01 25 14.6048	19.70	12.88		
SDSSJ015138.11+005559.1	4233-55449-587	0.4857	2.8007	01 51 38.1175	+00 55 59.1941	18.87	9.38		
SDSSJ015145.35-0000-1.3	3606-55182-695	0.4901	2.3563	01 51 45.3552	-00 00 -1.3063	19.00	11.47		
SDSSJ015150.88+143037.3	4657-55591-602	0.5623	2.2461	01 51 50.8855	+14 30 37.3569	19.18	26.54		
SDSSJ020103.73+161130.8	5119-55836-846	0.1110	2.9099	02 01 03.7308	+16 11 30.8203	16.13	16.03		
SDSSJ020241.40-064611.3	4398-55946-379	0.5020	2.7477	02 02 41.4084	-06 46 11.3322	19.40	12.55		
SDSSJ021742.02-002206.4	4236-55479-117	0.6069	2.4791	02 17 42.0209	-00 22 06.4687	19.46	13.00		
SDSSJ074502.39+181601.9	4488-55571- 49	0.5397	2.8723	07 45 02.3969	+18 16 01.9423	19.07	13.30		
SDSSJ074720.77+272914.9	4452-55536-205	0.2713	2.1796	07 47 20.7788	+27 29 14.9698	17.43	39.15		
SDSSJ074816.73+445602.8	3676-55186-623	0.5394	2.1854	07 48 16.7377	+44 56 02.8326	19.06	30.10		
SDSSJ074831.92+471014.4	3673-55178-795	0.4387	2.5056	07 48 31.9208	+47 10 14.4104	19.64	16.30		
SDSSJ075057.45+221035.8	4473-55589-231	0.4516	2.7564	07 50 57.4512	+22 10 35.8337	19.33	13.30		
SDSSJ075902.52+441705.0	3683-55178-662	0.4670	2.8857	07 59 02.5287	+44 17 05.0656	19.76	11.09		
SDSSJ075930.24+441245.5	3683-55245-671	0.4668	2.8857	07 59 30.2490	+44 12 45.5548	20.04	9.00		
SDSSJ081535.86+452133.5	3691-55274-138	0.5642	2.3773	08 15 35.8612	+45 21 33.5715	20.12	22.74		
SDSSJ081627.70+530140.5	3690-55182-643	0.5333	2.4243	08 16 27.7057	+53 01 40.5112	19.47	17.00		
SDSSJ082350.26+425114.1	3807-55511-153	0.6034	2.2890	08 23 50.2606	+42 51 14.1669	19.82	14.05		
SDSSJ082433.59+190704.5	4491-55570-827	0.5213	2.8821	08 24 33.5980	+19 07 04.5529	19.74	12.31		
SDSSJ083023.30+270017.9	4460-55533-583	0.5201	2.4235	08 30 23.3057	+27 00 17.9008	19.46	21.27		
SDSSJ083052.16+212858.1	4478-55600-135	0.6195	2.2626	08 30 52.1667	+21 28 58.1332	19.91	50.65		
SDSSJ083324.57+151215.4	4496-55544- 93	0.4501	1.9907	08 33 24.5728	+15 12 15.4488	19.57	54.92		
SDSSJ084211.29+383125.6	3765-55508-727	0.5816	2.8492	08 42 11.2903	+38 31 25.6934	19.57	61.33		
SDSSJ084246.17+362456.1	4609-56251-483	0.5169	2.8191	08 42 46.1719	+36 24 56.1044	19.57	16.90		
SDSSJ084300.13+194742.6	5176-56221-583	0.6985	2.5462	08 43 00.1392	+19 47 42.6251	19.81	16.72		
SDSSJ084443.21+012504.3	3810-55531-231	0.5911	2.7391	08 44 43.2129	+01 25 04.3223	20.00	8.58		
SDSSJ090254.78-005745.8	3818-55532-409	0.5786	2.8359	09 02 54.7888	-00 57 45.8659	19.43	9.08		
SDSSJ091526.15+585155.3	5712-56602-365	0.7812	2.8244	09 15 26.1548	+58 51 55.3244	19.83	13.72		
SDSSJ091727.90+250027.4	5777-56280-230	0.3261	2.4401	09 17 27.9089	+25 00 27.4658	18.19	13.36		
SDSSJ092133.07+363717.4	4644-55922-885	0.5558	2.6819	09 21 33.0762	+36 37 17.4069	19.91	15.66		
SDSSJ092159.66+070014.5	4870-55923-799	0.5903	2.2349	09 21 59.6631	+07 00 14.5483	19.62	17.31		
SDSSJ092335.14+190554.7	5767-56245-437	0.4387	2.5113	09 23 35.1416	+19 05 54.7485	18.45	14.97		
SDSSJ093551.05+085130.3	5314-55952-733	0.4569	2.5601	09 35 51.0498	+08 51 30.3065	19.55	18.46		
SDSSJ093741.40-013203.8	3767-55214-925	0.5094	2.9334	09 37 41.4038	-01 32 03.8081	19.70	16.27		
SDSSJ100149.69+273647.1	6471-56309-355	0.6218	2.1957	10 01 49.6985	+27 36 47.1602	19.61	14.55		
SDSSJ101908.39+250436.5	6465-56279-275	0.6473	2.4655	10 19 08.3936	+25 04 36.5190	19.09	13.18		
SDSSJ102529.98+424926.0	4557-55588-812	0.3413	2.6196	10 25 29.9890	+42 49 26.0339	17.75	11.08		
SDSSJ102901.22+472822.6	6659-56607-751	0.5696	2.8288	10 29 01.2268	+47 28 22.6337	19.11	19.70		
SDSSJ102938.39+154743.8	5340-56011-901	0.5607	2.1584	10 29 38.3899	+15 47 43.8268	19.61	34.94		
SDSSJ103117.27+262354.9	6457-56330-371	0.5478	2.7859	10 31 17.2778	+26 23 54.9586	19.68	11.49		
SDSSJ105018.46+090256.4	5354-55927-721	0.6180	2.4839	10 50 18.4680	+09 02 56.4404	19.56	12.61		
SDSSJ105222.56+472252.7	6664-56383-669	0.4747	2.2038	10 52 22.5659	+47 22 52.7417	18.96	11.57		
SDSSJ105507.57+314126.4	6445-56366-875	0.5189	2.4195	10 55 07.5769	+31 41 26.4670	19.93	18.60		
SDSSJ105620.82+114637.0	5356-55979-743	0.4698	2.2951	10 56 20.8228	+11 46 37.0264	19.90	15.66		
SDSSJ105752.35+064431.2	4854-55685-843	0.5961	2.9108	10 57 52.3572	+06 44 31.2948	19.44	10.59		
SDSSJ105909.96+110215.1	5356-55979-885	0.5459	2.6221	10 59 09.9609	+11 02 15.1524	18.89	18.03		
SDSSJ110148.19+523918.9	6706-56385-855	0.5821	2.8042	11 01 48.1970	+52 39 18.9294	19.87	8.05		
SDSSJ110502.65+035223.8	4771-55925-113	0.4929	2.7867	11 05 02.6514	+03 52 23.8632	19.54	7.40		

TABLE 2
Continued

Target	Plate-MJD-Fiber	z_L	z_s	R.A.		Decl.		m_i	Ly α Flux
SDSSJ111152.93+381222.2	4621-55649-257	0.5274	2.7503	11 11	52.9395	+38 12	22.2775	19.53	9.54
SDSSJ111544.57+084717.1	5366-55958-259	0.5523	2.8902	11 15	44.5715	+08 47	17.1574	19.54	15.83
SDSSJ111945.18+441146.0	6648-56383-253	0.6979	2.3540	11 19	45.1831	+44 11	46.0776	19.88	14.96
SDSSJ112159.89+525327.3	6698-56637-387	0.4655	2.1671	11 21	59.8938	+52 53	27.3486	19.87	35.11
SDSSJ112327.36+305352.6	6434-56362-705	0.4306	2.5137	11 23	27.3669	+30 53	52.6515	18.59	15.75
SDSSJ112429.08+583124.9	7100-56636-812	0.1960	2.3874	11 24	29.0881	+58 31	24.9518	17.60	12.78
SDSSJ112558.59+335647.1	4619-55599-680	0.4824	2.9216	11 25	58.5901	+33 56	47.1075	19.46	13.59
SDSSJ112708.12+652920.2	7110-56746-947	0.5358	2.6473	11 27	08.1226	+65 29	20.2020	19.48	14.23
SDSSJ113110.97+355020.7	4615-55618-399	0.4685	2.2974	11 31	10.9790	+35 50	20.7184	19.77	34.76
SDSSJ113938.99+165158.5	5891-56034-104	0.2791	2.4751	11 39	38.9978	+16 51	58.5242	17.89	46.45
SDSSJ114358.81+505552.1	6684-56412-835	0.5236	2.1737	11 43	58.8135	+50 55	52.1622	19.24	40.12
SDSSJ115136.39+233812.8	6423-56313-755	0.6404	2.9425	11 51	36.3977	+23 38	12.8398	19.94	9.50
SDSSJ115422.81-025127.8	3776-55209-451	0.5628	2.9018	11 54	22.8113	-02 51	27.8139	19.10	7.25
SDSSJ120047.44+423744.9	6634-56367-554	0.3335	2.8598	12 00	47.4463	+42 37	44.9139	18.32	26.65
SDSSJ120708.31+354719.6	4610-55621-789	0.5757	2.3012	12 07	08.3167	+35 47	19.6774	19.57	18.51
SDSSJ121559.87+043217.7	4749-55633-934	0.4847	2.8607	12 15	59.8718	+04 32	17.7377	19.73	14.47
SDSSJ122107.55+091612.1	5396-55947-145	0.4847	2.7798	12 21	07.5549	+09 16	12.1870	19.49	7.89
SDSSJ122440.53+222048.7	5982-56074-599	0.5051	2.7236	12 24	40.5322	+22 20	48.7335	19.57	14.69
SDSSJ122910.34+660924.4	7120-56720-417	0.5086	2.4109	12 29	10.3491	+66 09	24.4775	19.43	29.41
SDSSJ123248.00+622451.6	7118-56686-839	0.5796	2.1935	12 32	48.0066	+62 24	51.6824	19.65	30.68
SDSSJ123516.83-014605.4	3778-55213-319	0.5390	2.1920	12 35	16.8384	-01 46	05.4520	19.45	29.72
SDSSJ124132.92+253258.9	5984-56337-186	0.5372	2.7065	12 41	32.9224	+25 32	58.9055	19.40	21.57
SDSSJ124144.23+602441.0	6840-56685-377	0.5259	2.8350	12 41	44.2383	+60 24	41.0669	19.20	19.05
SDSSJ124300.16+262312.5	5984-56337-923	0.4504	2.8910	12 43	00.1648	+26 23	12.5652	18.78	17.27
SDSSJ125251.16+005805.7	3850-55575-653	0.5399	2.4345	12 52	51.1670	+00 58	05.7948	19.80	12.49
SDSSJ125424.73+235639.9	5989-56312-735	0.6689	2.5560	12 54	24.7375	+23 56	39.9458	19.82	17.02
SDSSJ125820.55+451139.1	6619-56371-904	0.4582	2.6481	12 58	20.5591	+45 11	39.1837	19.42	15.43
SDSSJ125847.45+072004.2	5417-55978-379	0.4700	2.5032	12 58	47.4573	+07 20	04.2801	19.07	18.73
SDSSJ125928.05+612722.1	6967-56447-575	0.4981	2.8741	12 59	28.0554	+61 27	22.1265	18.21	13.14
SDSSJ125941.63+024445.7	4005-55325-636	0.3350	2.4306	12 59	41.6382	+02 44	45.7256	18.21	11.78
SDSSJ130222.99+045135.2	4758-55682-734	0.4993	2.8483	13 02	22.9980	+04 51	35.2693	19.52	11.54
SDSSJ132159.23+301023.4	6489-56329-661	0.4468	2.4631	13 21	59.2346	+30 10	23.4810	19.69	10.21
SDSSJ132525.47+393914.5	4707-55653-211	0.5082	2.8280	13 25	25.4700	+39 39	14.5486	19.81	11.33
SDSSJ132530.49+032328.3	4761-55633- 55	0.4799	2.5226	13 25	30.4980	+03 23	28.3434	19.31	12.16
SDSSJ132808.67+615717.6	6817-56455-897	0.5310	2.1957	13 28	08.6792	+61 57	17.6358	19.63	29.19
SDSSJ134225.98+444856.1	6628-56366-651	0.6208	2.1468	13 42	25.9827	+44 48	56.1099	19.57	22.94
SDSSJ134403.20+364645.7	3852-55243-491	0.4582	2.7911	13 44	03.2080	+36 46	45.7159	19.39	26.13
SDSSJ134408.02+162127.9	5439-56045-109	0.4957	2.3610	13 44	08.0200	+16 21	27.9890	19.28	49.16
SDSSJ134535.17+470306.6	6749-56370-435	0.5260	2.6196	13 45	35.1782	+47 03	06.6714	19.65	18.89
SDSSJ140455.24+460020.4	6750-56367-171	0.4588	2.4727	14 04	55.2466	+46 00	20.4620	19.16	9.72
SDSSJ140639.02-020526.4	4038-55363-819	0.5304	2.7589	14 06	39.0234	-02 05	26.4441	19.73	8.94
SDSSJ141026.39+212852.3	5896-56047-358	0.3135	2.9470	14 10	26.3965	+21 28	52.3036	18.18	16.46
SDSSJ141358.21+293240.4	6497-56329-271	0.4461	2.7151	14 13	58.2129	+29 32	40.4073	19.41	17.63
SDSSJ141613.97+301457.0	6497-56329-843	0.5666	2.3858	14 16	13.9709	+30 14	57.0543	19.50	5.82
SDSSJ141815.72+015832.2	4030-55634-117	0.5559	2.1388	14 18	15.7288	+01 58	32.2270	19.35	28.14
SDSSJ142006.70+320348.3	3867-55652-544	0.7268	2.7780	14 20	06.7017	+32 03	48.3234	19.66	12.98
SDSSJ142516.87+142856.5	5461-56018-142	0.3710	2.4583	14 25	16.8750	+14 28	56.4956	18.46	9.16
SDSSJ142823.28+235839.2	6014-56072-764	0.4660	2.7911	14 28	23.2874	+23 58	39.2230	19.36	18.49
SDSSJ142954.80+120235.5	5463-56003-121	0.5531	2.8253	14 29	54.8035	+12 02	35.5836	19.60	25.57
SDSSJ143133.29-004454.1	4025-55350-449	0.4400	2.4480	14 31	33.2959	-00 44	54.1727	21.07	46.76
SDSSJ143316.32+511222.0	6718-56398-321	0.5323	2.5997	14 33	16.3257	+51 12	22.0853	19.46	19.36
SDSSJ143719.80+335056.1	3865-55272-411	0.4725	2.2792	14 37	19.8083	+33 50	56.1356	18.99	7.85
SDSSJ144021.10+200416.9	5904-56046-363	0.5452	2.2529	14 40	21.1084	+20 04	16.9359	19.91	23.85
SDSSJ144317.83+510721.0	6725-56390-772	0.5501	2.9443	14 43	17.8381	+51 07	21.0187	18.72	16.88
SDSSJ144320.72+334212.1	3865-55272- 67	0.5786	2.2016	14 43	20.7275	+33 42	12.1014	19.56	54.20
SDSSJ144431.48+371139.7	5173-56046- 85	0.4873	2.1913	14 44	31.4832	+37 11	39.7192	19.40	17.68
SDSSJ150114.60+304230.8	3875-55364-935	0.6384	2.6498	15 01	14.6082	+30 42	30.8537	19.44	14.96
SDSSJ150221.28-001425.6	4016-55632-383	0.6272	2.2230	15 02	21.2805	-00 14	25.6128	19.76	28.97
SDSSJ150256.13+382017.8	5168-56035-693	0.4531	2.6692	15 02	56.1328	+38 20	17.8894	18.74	19.59
SDSSJ151017.06+193935.8	3956-55656-289	0.5222	2.9298	15 10	17.0618	+19 39	35.8621	19.58	12.96

TABLE 2
Continued

Target	Plate-MJD-Fiber	z_L	z_s	R.A.	Decl.	m_i	Ly α Flux
SDSSJ151921.73+242649.7	3961-55654-899	0.4608	2.9434	15 19 21.7310	+24 26 49.7786	18.72	9.47
SDSSJ152105.06+254110.0	3964-55648- 61	0.5987	2.4306	15 21 05.0684	+25 41 10.0081	19.65	23.06
SDSSJ152851.87+310233.8	4723-56033-445	0.7426	2.1482	15 28 51.8701	+31 02 33.8910	19.45	15.76
SDSSJ153635.76+024211.9	4054-55358-721	0.5169	2.1774	15 36 35.7642	+02 42 11.9110	19.27	19.96
SDSSJ153808.49+063010.6	4885-55735- 15	0.5296	2.8332	15 38 08.4961	+06 30 10.6894	19.61	17.62
SDSSJ154204.99+401954.6	4976-56046-672	0.4351	2.4976	15 42 04.9951	+40 19 54.6945	18.78	38.28
SDSSJ154533.14+114438.4	4886-55737-229	0.5087	2.2845	15 45 33.1494	+11 44 38.4325	19.10	13.13
SDSSJ154611.14+280542.5	3952-55330-944	0.3044	2.7125	15 46 11.1438	+28 05 42.5880	17.95	17.26
SDSSJ155458.11+264630.7	3946-55659-954	0.2914	2.4440	15 54 58.1177	+26 46 30.7333	17.79	12.73
SDSSJ155821.52+265829.7	4725-55711-295	0.5788	2.3788	15 58 21.5222	+26 58 29.7679	19.66	24.13
SDSSJ160007.29+145112.2	3923-55325-932	0.3416	2.3649	16 00 07.2986	+14 51 12.2340	18.14	12.08
SDSSJ160324.84+203108.4	3924-55332-559	0.5527	2.1657	16 03 24.8438	+20 31 08.4723	19.76	30.28
SDSSJ160348.28+443842.4	6034-56103-572	0.4823	2.6138	16 03 48.2849	+44 38 42.4411	19.28	12.41
SDSSJ161514.04+094650.7	5205-56040-279	0.4643	2.5324	16 15 14.0442	+09 46 50.7319	19.49	12.35
SDSSJ162432.12+524049.6	6313-56460-757	0.3707	2.8857	16 24 32.1277	+52 40 49.6765	19.45	10.99
SDSSJ165003.84+494249.8	6315-56181-654	0.3889	2.6861	16 50 03.8489	+49 42 49.8120	18.15	7.38
SDSSJ172646.46+270324.9	5004-55711-565	0.5633	2.0505	17 26 46.4648	+27 03 24.9019	19.38	31.25
SDSSJ173225.89+264240.3	5004-55711-151	0.5029	2.1957	17 32 25.8911	+26 42 40.3294	19.93	12.43
SDSSJ212047.63-000911.3	4192-55469-151	0.5470	2.6590	21 20 47.6367	-00 09 11.3327	19.94	27.13
SDSSJ212932.71+080751.9	4085-55452-895	0.4139	2.5316	21 29 32.7173	+08 07 51.9658	18.44	20.20
SDSSJ214843.04+044436.1	4091-55498-227	0.6584	2.6963	21 48 43.0444	+04 44 36.1066	19.85	10.03
SDSSJ215034.63+245016.5	5960-56097-209	0.5039	2.2822	21 50 34.6362	+24 50 16.5367	19.10	13.36
SDSSJ221321.15+090241.0	5068-55749-829	0.6295	2.6666	22 13 21.1523	+09 02 41.0630	19.79	15.83
SDSSJ221952.65+104226.6	5047-55833-169	0.5029	2.2230	22 19 52.6538	+10 42 26.6000	19.29	18.09
SDSSJ222151.54+072400.2	5069-56211-141	0.7507	2.5072	22 21 51.5479	+07 24 00.2355	19.64	13.67
SDSSJ222234.29+200711.6	5023-55858-985	0.6448	2.4528	22 22 34.2920	+20 07 11.6048	19.88	11.16
SDSSJ223301.06+100921.6	5053-56213-894	0.5684	2.4456	22 33 01.0693	+10 09 21.6623	19.71	28.09
SDSSJ223333.16+272037.5	6297-56218-817	0.5324	2.6963	22 33 33.1641	+27 20 37.5412	19.86	10.90
SDSSJ223622.28+272332.8	6297-56218-923	0.5299	2.8474	22 36 22.2803	+27 23 32.8281	19.90	14.63
SDSSJ223843.98+151959.4	5038-56235- 77	0.5717	2.3057	22 38 43.9819	+15 19 59.4942	20.04	18.58
SDSSJ224704.56+162549.5	5033-56244-339	0.2927	2.3936	22 47 04.5630	+16 25 49.5117	18.80	72.74
SDSSJ224746.60-024237.9	4364-55855-469	0.4176	2.7720	22 47 46.6040	-02 42 37.8978	19.35	11.56
SDSSJ230217.65+302738.2	6506-56564-729	0.5612	2.8060	23 02 17.6514	+30 27 38.2901	19.78	13.51
SDSSJ230827.85+311814.9	6504-56540-258	0.4096	2.6515	23 08 27.8540	+31 18 14.9936	18.69	378.79
SDSSJ230917.33+072438.6	6168-56187-395	0.5606	2.2883	23 09 17.3364	+07 24 38.6568	19.48	18.67
SDSSJ231418.03-011027.0	4209-55478-171	0.5221	2.2679	23 14 18.0322	-01 10 27.0288	19.85	20.38
SDSSJ231731.62+115450.9	6147-56239-163	0.5448	2.6389	23 17 31.6260	+11 54 50.9168	19.62	38.16
SDSSJ232231.78+144340.7	6143-56267-511	0.4522	2.4062	23 22 31.7871	+14 43 40.7233	18.93	13.05
SDSSJ233240.44+150308.2	6137-56270-331	0.5096	2.3695	23 32 40.4443	+15 03 08.1958	19.73	21.74
SDSSJ233311.11+022310.9	4282-55507-607	0.4716	2.2529	23 33 11.1182	+02 23 10.9309	19.92	24.45
SDSSJ234617.29+090931.4	6160-56190-854	0.1817	2.7125	23 46 17.2925	+09 09 31.4367	17.35	27.96
SDSSJ234653.04-032113.7	4356-55829-185	0.6154	2.7841	23 46 53.0420	-03 21 13.6990	19.97	19.92
SDSSJ235212.72+214526.1	6521-56537-324	0.5133	2.9180	23 52 12.7222	+21 45 26.1749	19.74	14.22
SDSSJ235356.11-083238.8	7166-56602-783	0.4790	2.6038	23 53 56.1108	-08 32 38.8589	19.27	13.98
SDSSJ235508.04-052826.7	7033-56565-257	0.5572	2.5178	23 55 08.0493	-05 28 26.7535	19.71	8.76
SDSSJ235525.24-052138.6	7033-56565-181	0.4917	2.2431	23 55 25.2466	-05 21 38.6252	19.28	13.67